

Time-resolved high harmonic spectroscopy of dynamical symmetry breaking in bi-circular laser fields

ÁLVARO JIMÉNEZ-GALÁN,^{1,*} NICKOLAI ZHAVORONKOV,¹ MARCEL SCHLOZ,¹ FELIPE MORALES,¹ AND MISHA IVANOV^{1,2,3}

¹Max-Born Institute for Nonlinear Optics and Short Pulse Spectroscopy, Max-Born-Straße 2A, D-12489 Berlin, Germany

²Institute für Physik, Humboldt-Universität zu Berlin, Newtonstraße 15, D-12489 Berlin, Germany

³Department of Physics, Imperial College London, South Kensington Campus, SW72AZ London, UK
*jimenez@mbi-berlin.de

Abstract: The bi-circular scheme for high harmonic generation, which combines two counter-rotating circular fields with frequency ratio 2:1, has recently permitted to generate high harmonics with essentially circular polarization, opening the way for ultrafast chiral studies. This scheme produces harmonic lines at $3N + 1$ and $3N + 2$ multiples of the fundamental driving frequency, while the $3N$ lines are forbidden owing to the three-fold symmetry of the field. It is generally established that the routinely observed signals at these forbidden harmonic lines come from a slight ellipticity in the driving fields, which breaks the three-fold symmetry. We find that this is neither the only nor it is the dominant mechanism responsible. The forbidden lines can be observed even for perfectly circular, long driving pulses. We show that they encode rich information on the sub-cycle electronic dynamics that occur during the generation process. By varying the time delay and relative intensity between the two drivers, we demonstrate that when the second harmonic either precedes or is more intense than the fundamental field, the dynamical symmetry of the system is broken by electrons trapped in Rydberg orbits (i.e., Freeman resonances), and that the forbidden harmonic lines are a witness of this.

© 2021 Optical Society of America

OCIS codes: (190.4160) Multi harmonic generation; (020.2649) Strong-field laser physics; (020.4180) Multiphoton processes; (320.7110) Ultrafast nonlinear optics.

References and links

1. F. Krausz and M. Ivanov, "Attosecond physics," *Reviews of Modern Physics* **81**, 163–234 (2009).
2. G. Sansone, F. Kelkensberg, J. F. Pérez-Torres, F. Morales, M. F. Kling, W. Siu, O. Ghafur, P. Johnsson, M. Swoboda, E. Benedetti, F. Ferrari, F. Lepine, J. L. Sanz-Vicario, S. Zherebtsov, I. Znakovskaya, A. L'Huillier, M. Y. Ivanov, M. Nisoli, F. Martin, and M. J. J. Vrakking, "Electron localization following attosecond molecular photoionization," *Nature* **465**, 763–766 (2010).
3. V. Gruson, L. Barreau, Á. Jiménez-Galan, F. Risoud, J. Caillat, A. Maquet, B. Carré, F. Lepetit, J. F. Hergott, T. Ruchon, L. Argenti, R. Taïeb, F. Martín, and P. Salières, "Attosecond dynamics through a fano resonance: Monitoring the birth of a photoelectron," *Science* **354**, 734 (2016).
4. F. Kelkensberg, W. Siu, J. F. Pérez-Torres, F. Morales, G. Gademann, A. Rouzée, P. Johnsson, M. Lucchini, F. Calegari, J. L. Sanz-Vicario, F. Martín, and M. J. J. Vrakking, "Attosecond control in photoionization of hydrogen molecules," *Physical Review Letters* **107**, 043002– (2011).
5. M. T. Hassan, T. T. Luu, A. Moulet, O. Raskazovskaya, P. Zhokhov, M. Garg, N. Karpowicz, A. M. Zheltikov, V. Pervak, F. Krausz, and E. Goulielmakis, "Optical attosecond pulses and tracking the nonlinear response of bound electrons," *Nature* **530**, 66–70 (2016).
6. M. Garg, M. Zhan, T. T. Luu, H. Lakhota, T. Klostermann, A. Guggenmos, and E. Goulielmakis, "Multi-petahertz electronic metrology," *Nature* **538**, 359–363 (2016).
7. S. Baker, J. S. Robinson, C. Haworth, H. Teng, R. Smith, C. Chirilă, M. Lein, J. Tisch, and J. P. Marangos, "Probing proton dynamics in molecules on an attosecond time scale," *Science* **312**, 424–427 (2006).
8. O. Smirnova, Y. Mairesse, S. Patchkovskii, N. Dudovich, D. Villeneuve, P. Corkum, and M. Y. Ivanov, "High harmonic interferometry of multi-electron dynamics in molecules," *Nature* **460**, 972–977 (2009).
9. S. Haessler, J. Caillat, W. Boutu, C. Giovanetti-Teixeira, T. Ruchon, T. Auguste, Z. Diveki, P. Breger, A. Maquet, B. Carre, R. Taïeb, and P. Salieres, "Attosecond imaging of molecular electronic wavepackets," *Nat Phys* **6**, 200–206 (2010).

10. C. Vozzi, M. Negro, F. Calegari, G. Sansone, M. Nisoli, S. De Silvestri, and S. Stagira, "Generalized molecular orbital tomography," *Nature Physics* **7**, 822–826 (2011).
11. D. Shafir, H. Soifer, B. D. Bruner, M. Dagan, Y. Mairesse, S. Patchkovskii, M. Y. Ivanov, O. Smirnova, and N. Dudovich, "Resolving the time when an electron exits a tunnelling barrier," *Nature* **485**, 343–346 (2012).
12. H. Wörner, J. Bertrand, D. Kartashov, P. Corkum, and D. Villeneuve, "Following a chemical reaction using high-harmonic interferometry," *Nature* **466**, 604–607 (2010).
13. A. Ferré, H. Soifer, O. Pedatzur, C. Bourassin-Bouchet, B. D. Bruner, R. Canonge, F. Catoire, D. Descamps, B. Fabre, E. Mével, S. Petit, N. Dudovich, and Y. Mairesse, "Two-dimensional frequency resolved optomolecular gating of high-order harmonic generation," *Physical Review Letters* **116**, 053002– (2016).
14. F. Morales, I. Barth, V. Serbinenko, S. Patchkovskii, and O. Smirnova, "Shaping polarization of attosecond pulses via laser control of electron and hole dynamics," *Journal of Modern Optics* **59**, 1303–1311 (2012).
15. O. Pedatzur, G. Orenstein, V. Serbinenko, H. Soifer, B. D. Bruner, A. J. Uzan, D. S. Brambila, A. G. Harvey, L. Torlina, F. Morales, O. Smirnova, and N. Dudovich, "Attosecond tunnelling interferometry," *Nat Phys* **11**, 815–819 (2015).
16. B. D. Bruner, H. Soifer, D. Shafir, V. Serbinenko, O. Smirnova, and N. Dudovich, "Multidimensional high harmonic spectroscopy," *Journal of Physics B: Atomic, Molecular and Optical Physics* **48**, 174006 (2015).
17. B. D. Bruner, Z. Masin, M. Negro, F. Morales, D. Brambila, M. Devetta, D. Facciala, A. G. Harvey, M. Ivanov, Y. Mairesse, S. Patchkovskii, V. Serbinenko, H. Soifer, S. Stagira, C. Vozzi, N. Dudovich, and O. Smirnova, "Multidimensional high harmonic spectroscopy of polyatomic molecules: detecting sub-cycle laser-driven hole dynamics upon ionization in strong mid-ir laser fields," *Faraday Discuss.* **194**, 369–405 (2016).
18. V. Serbinenko and O. Smirnova, "Multidimensional high harmonic spectroscopy: a semi-classical perspective on measuring multielectron rearrangement upon ionization," *Journal of Physics B: Atomic, Molecular and Optical Physics* **46**, 171001 (2013).
19. O. Smirnova, Y. Mairesse, and S. Patchkovskii, "Opportunities for chiral discrimination using high harmonic generation in tailored laser fields," *Journal of Physics B: Atomic, Molecular and Optical Physics* **48**, 234005 (2015).
20. P. M. Kraus, B. Mignolet, D. Baykusheva, A. Rupenyan, L. Horný, E. F. Penka, G. Grassi, O. I. Tolstikhin, J. Schneider, F. Jensen, L. B. Madsen, A. D. Bandrauk, F. Remacle, and H. J. Wörner, "Measurement and laser control of attosecond charge migration in ionized iodoacetylene," *Science* **350**, 790–795 (2015).
21. H. J. Wörner, J. B. Bertrand, B. Fabre, J. Higuette, H. Ruf, A. Dubrouil, S. Patchkovskii, M. Spanner, Y. Mairesse, V. Blanchet, E. Mével, E. Constant, P. B. Corkum, and D. M. Villeneuve, "Conical intersection dynamics in NO_2 probed by homodyne high-harmonic spectroscopy," *Science* **334**, 208 (2011).
22. S. Ghimire, A. D. DiChiara, E. Sistrunk, P. Agostini, L. F. DiMauro, and D. A. Reis, "Observation of high-order harmonic generation in a bulk crystal," *Nature physics* **7**, 138–141 (2011).
23. A. Schiffrin, T. Paasch-Colberg, N. Karpowicz, V. Apalkov, D. Gerster, S. Muhlbrandt, M. Korbman, J. Reichert, M. Schultze, S. Holzner, J. V. Barth, R. Kienberger, R. Ernstorfer, V. S. Yakovlev, M. I. Stockman, and F. Krausz, "Optical-field-induced current in dielectrics," *Nature* **493**, 70–74 (2013).
24. M. Ivanov and O. Smirnova, "Opportunities for sub-laser-cycle spectroscopy in condensed phase," *Chemical Physics* **414**, 3–9 (2013).
25. G. Vampa, C. McDonald, G. Orlando, D. Klug, P. Corkum, and T. Brabec, "Theoretical analysis of high-harmonic generation in solids," *Physical review letters* **113**, 073901 (2014).
26. G. Vampa, T. Hammond, N. Thiré, B. Schmidt, F. Légaré, C. McDonald, T. Brabec, and P. Corkum, "Linking high harmonics from gases and solids," *Nature* **522**, 462–464 (2015).
27. F. Langer, M. Hohenleutner, C. P. Schmid, C. Poellmann, P. Nagler, T. Korn, C. Schüller, M. S. Sherwin, U. Huttner, J. T. Steiner, S. W. Koch, M. Kira, and R. Huber, "Lightwave-driven quasiparticle collisions on a subcycle timescale," *Nature* **533**, 225–229 (2016).
28. H. Eichmann, A. Egbert, S. Nolte, C. Momma, B. Wellegehausen, W. Becker, S. Long, and J. K. McIver, "Polarization-dependent high-order two-color mixing," *Physical Review A* **51**, R3414–R3417 (1995).
29. D. B. Milošević, W. Becker, and R. Kopold, "Generation of circularly polarized high-order harmonics by two-color coplanar field mixing," *Physical Review A* **61**, 063403– (2000).
30. A. Fleischer, O. Kfir, T. Diskin, P. Sidorenko, and O. Cohen, "Spin angular momentum and tunable polarization in high-harmonic generation," *Nature Photonics* **8**, 543–549 (2014).
31. C. Chen, Z. Tao, C. Hernández-García, P. Matyba, A. Carr, R. Knut, O. Kfir, D. Zusin, C. Gentry, P. Grychtol, O. Cohen, L. Plaja, A. Becker, A. Jaron-Becker, H. Kapteyn, and M. Murnane, "Tomographic reconstruction of circularly polarized high-harmonic fields: 3d attosecond metrology," *Science Advances* **2** (2016).
32. D. D. Hickstein, F. J. Dollar, P. Grychtol, J. L. Ellis, R. Knut, C. Hernández-García, D. Zusin, C. Gentry, J. M. Shaw, T. Fan, K. M. Dorney, A. Becker, A. Jaron-Becker, H. C. Kapteyn, M. M. Murnane, and C. G. Durfee, "Non-collinear generation of angularly isolated circularly polarized high harmonics," *Nat Photon* **9**, 743–750 (2015).
33. O. Kfir, P. Grychtol, E. Turgut, R. Knut, D. Zusin, D. Popmintchev, T. Popmintchev, H. Nembach, J. M. Shaw, A. Fleischer, H. Kapteyn, M. Murnane, and O. Cohen, "Generation of bright phase-matched circularly-polarized extreme ultraviolet high harmonics," *Nat Photon* **9**, 99–105 (2015).
34. D. Baykusheva, M. S. Ahsan, N. Lin, and H. J. Wörner, "Bicircular high-harmonic spectroscopy reveals dynamical symmetries of atoms and molecules," *Physical Review Letters* **116**, 123001– (2016).
35. A. D. Bandrauk, F. Mauger, and K.-J. Yuan, "Circularly polarized harmonic generation by intense bicircular laser pulses: electron recollision dynamics and frequency dependent helicity," *Journal of Physics B: Atomic, Molecular*

- and Optical Physics **49**, 23LT01 (2016).
36. F. Mauger, A. Bandrauk, and T. Uzer, "Circularly polarized molecular high harmonic generation using a bicircular laser," *Journal of Physics B: Atomic, Molecular and Optical Physics* **49**, 10LT01 (2016).
 37. S. Odžak, E. Hasović, W. Becker, and D. Milošević, "Atomic processes in bicircular fields," *Journal of Modern Optics* pp. 1–10 (2016).
 38. S. Odžak, E. Hasović, and D. B. Milošević, "High-order harmonic generation in polyatomic molecules induced by a bicircular laser field," *Physical Review A* **94**, 033419 (2016).
 39. T. Fan, P. Grychtol, R. Knut, C. Hernández-García, D. D. Hickstein, D. Zusin, C. Gentry, F. J. Dollar, C. A. Mancuso, C. W. Hogle, O. Kfir, D. Legut, K. Carva, J. L. Ellis, K. M. Dorney, C. Chen, O. G. Shpyrko, E. E. Fullerton, O. Cohen, P. M. Oppeneer, D. B. Milošević, A. Becker, A. A. Jaroń-Becker, T. Popmintchev, M. M. Murnane, and H. C. Kapteyn, "Bright circularly polarized soft x-ray high harmonics for x-ray magnetic circular dichroism," *Proceedings of the National Academy of Sciences* **112**, 14206–14211 (2015).
 40. D. B. Milošević, "Generation of elliptically polarized attosecond pulse trains," *Optics Letters* **40**, 2381–2384 (2015).
 41. L. Medžišauskas, J. Wragg, H. van der Hart, and M. Y. Ivanov, "Generating isolated elliptically polarized attosecond pulses using bichromatic counterrotating circularly polarized laser fields," *Physical Review Letters* **115**, 153001–(2015).
 42. X. Zhang, X. Zhu, X. Liu, D. Wang, Q. Zhang, P. Lan, and P. Lu, "Ellipticity-tunable attosecond xuv pulse generation with a rotating bichromatic circularly polarized laser field," *Optics Letters* **42**, 1027–1030 (2017).
 43. R. Cireasa, A. E. Boguslavskiy, B. Pons, M. C. H. Wong, D. Descamps, S. Petit, H. Ruf, N. Thire, A. Ferre, J. Suarez, J. Higuier, B. E. Schmidt, A. F. Alharbi, F. Legare, V. Blanchet, B. Fabre, S. Patchkovskii, O. Smirnova, Y. Mairesse, and V. R. Bhardwaj, "Probing molecular chirality on a sub-femtosecond timescale," *Nat Phys* **11**, 654–658 (2015).
 44. A. L. Cavalieri, N. Müller, T. Uphues, V. S. Yakovlev, A. Baltuska, B. Horvath, B. Schmidt, L. Blumel, R. Holzwarth, S. Hendel, M. Drescher, U. Kleineberg, P. M. Echenique, R. Kienberger, F. Krausz, and U. Heinzmann, "Attosecond spectroscopy in condensed matter," *Nature* **449**, 1029–1032 (2007).
 45. C. Boeglin, E. Beaurepaire, V. Halte, V. Lopez-Flores, C. Stamm, N. Pontius, H. A. Dürr, and J. Y. Bigot, "Distinguishing the ultrafast dynamics of spin and orbital moments in solids," *Nature* **465**, 458–461 (2010).
 46. C. E. Graves, A. H. Reid, T. Wang, B. Wu, S. de Jong, K. Vahaplar, I. Radu, D. P. Bernstein, M. Messerschmidt, L. Müller, R. Coffee, M. Bionta, S. W. Epp, R. Hartmann, N. Kimmel, G. Hauser, A. Hartmann, P. Holl, H. Gorke, J. H. Mentink, A. Tsukamoto, A. Fognini, J. J. Turner, W. F. Schlotter, D. Rolles, H. Soltau, L. Strüder, Y. Acremann, A. V. Kimel, A. Kirilyuk, T. Rasing, J. Stöhr, A. O. Scherz, and H. A. Dürr, "Nanoscale spin reversal by non-local angular momentum transfer following ultrafast laser excitation in ferrimagnetic gdfeco," *Nat Mater* **12**, 293–298 (2013).
 47. N. Dudovich, O. Smirnova, J. Levesque, Y. Mairesse, M. Y. Ivanov, D. Villeneuve, and P. B. Corkum, "Measuring and controlling the birth of attosecond xuv pulses," *Nature physics* **2**, 781–786 (2006).
 48. E. Mansten, J. M. Dahlström, P. Johnsson, M. Swoboda, A. L'Huillier, and J. Mauritsson, "Spectral shaping of attosecond pulses using two-colour laser fields," *New Journal of Physics* **10**, 083041 (2008).
 49. J. Mauritsson, J. Dahlström, E. Mansten, and T. Fordell, "Sub-cycle control of attosecond pulse generation using two-colour laser fields," *Journal of Physics B: Atomic, Molecular and Optical Physics* **42**, 134003 (2009).
 50. X. He, J. Dahlström, R. Rakowski, C. Heyl, A. Persson, J. Mauritsson, and A. L'Huillier, "Interference effects in two-color high-order harmonic generation," *Physical Review A* **82**, 033410 (2010).
 51. J. Dahlström, A. L'Huillier, and J. Mauritsson, "Quantum mechanical approach to probing the birth of attosecond pulses using a two-colour field," *Journal of Physics B: Atomic, Molecular and Optical Physics* **44**, 095602 (2011).
 52. L. Brugnera, D. J. Hoffmann, T. Siegel, F. Frank, A. Zaïr, J. W. Tisch, and J. P. Marangos, "Trajectory selection in high harmonic generation by controlling the phase between orthogonal two-color fields," *Physical review letters* **107**, 153902 (2011).
 53. R. Ganeev, V. Strelkov, C. Hutchison, A. Zaïr, D. Kilbane, M. Khokhlova, and J. Marangos, "Experimental and theoretical studies of two-color-pump resonance-induced enhancement of odd and even harmonics from a tin plasma," *Physical Review A* **85**, 023832 (2012).
 54. M. Y. Ivanov, P. Corkum, and P. Dietrich, "Coherent control and collapse of symmetry in a two-level system in an intense laser field," *Laser Physics* **3**, 375–380 (1993).
 55. O. Smirnova, M. Spanner, and M. Ivanov, "Anatomy of strong field ionization ii: to dress or not to dress?" *Journal of Modern Optics* **54**, 1019–1038 (2007).
 56. F. Morales, P. Rivière, M. Richter, A. Gubaydullin, M. Ivanov, O. Smirnova, and F. Martín, "High harmonic spectroscopy of electron localization in the hydrogen molecular ion," *Journal of Physics B: Atomic, Molecular and Optical Physics* **47**, 204015 (2014).
 57. X.-B. Bian and A. D. Bandrauk, "Probing nuclear motion by frequency modulation of molecular high-order harmonic generation," *Physical review letters* **113**, 193901 (2014).
 58. R. E. F. Silva, P. Rivière, F. Morales, O. Smirnova, M. Ivanov, and F. Martín, "Even harmonic generation in isotropic media of dissociating homonuclear molecules," *Scientific Reports* **6**, 32653 (2016).
 59. G. L. Yudin and M. Y. Ivanov, "Physics of correlated double ionization of atoms in intense laser fields: Quasistatic tunneling limit," *Physical Review A* **63**, 033404 (2001).
 60. T. Nubbemeyer, K. Gorling, A. Saenz, U. Eichmann, and W. Sandner, "Strong-field tunneling without ionization," *Physical review letters* **101**, 233001 (2008).

61. U. Eichmann, T. Nubbemeyer, H. Rottke, and W. Sandner, "Acceleration of neutral atoms in strong short-pulse laser fields," *Nature* **461**, 1261–1264 (2009).
62. A. von Veltheim, B. Manschwetus, W. Quan, B. Borchers, G. Steinmeyer, H. Rottke, and W. Sandner, "Frustrated tunnel ionization of noble gas dimers with rydberg-electron shakeoff by electron charge oscillation," *Physical review letters* **110**, 023001 (2013).
63. U. Eichmann, A. Saenz, S. Eilzer, T. Nubbemeyer, and W. Sandner, "Observing rydberg atoms to survive intense laser fields," *Physical review letters* **110**, 203002 (2013).
64. H. Zimmermann, S. Patchkovskii, M. Ivanov, and U. Eichmann, "Unified time and frequency picture of ultrafast atomic excitation in strong laser fields," *Physical Review Letters* **118**, 013003 (2017).
65. M. Richter, S. Patchkovskii, F. Morales, O. Smirnova, and M. Ivanov, "The role of the kramers–henneberger atom in the higher-order kerr effect," *New Journal of Physics* **15**, 083012 (2013).
66. A. Popov, O. Tikhonova, and E. Volkova, "Strong-field atomic stabilization: numerical simulation and analytical modelling," *Journal of Physics B: Atomic, Molecular and Optical Physics* **36**, R125 (2003).
67. A. Popov, O. Tikhonova, and E. Volkova, "Different regimes of strong-field dynamics of atoms in intense low-frequency laser pulses," *Journal of Modern Optics* **58**, 1195–1205 (2011).
68. M. V. Fedorov, N. P. Poluektov, A. M. Popov, O. V. Tikhonova, V. Y. Kharin, and E. A. Volkova, "Interference stabilization revisited," *IEEE Journal of Selected Topics in Quantum Electronics* **18**, 42–53 (2012).
69. F. Morales, M. Richter, S. Patchkovskii, and O. Smirnova, "Imaging the kramers–henneberger atom," *Proceedings of the National Academy of Sciences* **108**, 16906–16911 (2011).
70. T. Bredtmann, S. Chelkowski, A. D. Bandrauk, and M. Ivanov, "Xuv lasing during strong-field-assisted transient absorption in molecules," *Physical Review A* **93**, 021402 (2016).
71. G. L. Yudin and M. Y. Ivanov, "Physics of correlated double ionization of atoms in intense laser fields: Quasistatic tunneling limit," *Physical Review A* **63**, 033404– (2001).
72. B. Manschwetus, T. Nubbemeyer, K. Gorling, G. Steinmeyer, U. Eichmann, H. Rottke, and W. Sandner, "Strong laser field fragmentation of h₂: Coulomb explosion without double ionization," *Physical review letters* **102**, 113002 (2009).
73. P. Agostini and L. F. DiMauro, "The physics of attosecond light pulses," *Reports on progress in physics* **67**, 813 (2004).
74. K. Ishikawa, "Photoemission and ionization of $\{\mathrm{h}\}\mathrm{e}^{\{+\}}$ under simultaneous irradiation of fundamental laser and high-order harmonic pulses," *Physical Review Letters* **91**, 043002– (2003).
75. O. Kornilov, R. Wilcox, and O. Gessner, "Nanograting-based compact vacuum ultraviolet spectrometer and beam profile for in situ characterization of high-order harmonic generation light sources," *Review of Scientific Instruments* **81**, 063109–063112 (2010).
76. S. Patchkovskii and H. G. Muller, "Simple, accurate, and efficient implementation of 1-electron atomic time-dependent schrödinger equation in spherical coordinates," *Computer Physics Communications* **199**, 153–169 (2016).
77. X. M. Tong and C. D. Lin, "Empirical formula for static field ionization rates of atoms and molecules by lasers in the barrier-suppression regime," *Journal of Physics B: Atomic, Molecular and Optical Physics* **38**, 2593 (2005).
78. F. Morales, T. Bredtmann, and S. Patchkovskii, "isurf: a family of infinite-time surface flux methods," *Journal of Physics B: Atomic, Molecular and Optical Physics* **49**, 245001 (2016).
79. G. N. Gibson, R. R. Freeman, and T. J. McIlrath, "Verification of the dominant role of resonant enhancement in short-pulse multiphoton ionization," *Physical Review Letters* **69**, 1904–1907 (1992).
80. G. N. Gibson, R. R. Freeman, T. J. McIlrath, and H. G. Muller, "Excitation and ionization dynamics in short-pulse multiphoton ionization," *Physical Review A* **49**, 3870–3874 (1994).

1. Introduction

High harmonic generation serves as an indispensable source of bright, coherent XUV and soft X-ray light. This light is used to induce, monitor and control the dynamics of electrons in atoms, molecules and solids at their intrinsic timescale [1–6]. High harmonic generation also serves as a spectroscopic tool for unraveling the complex multi-electron and coupled electron-nuclear dynamics in molecules [7–21] and solids [22–27].

From the light source perspective, high harmonic generation in two counter-rotating circularly polarized fields made by superposing the fundamental field ω and its second harmonic 2ω [28,29] is particularly appealing [30–39]. It allows one to generate XUV radiation and trains of attosecond pulses with controlled polarization properties [29,30,40] and carries the potential to generate isolated circularly polarized attosecond pulses [41,42]. These pulses would open the route to studying chiral-sensitive light-matter interactions with unprecedented temporal resolution in gas and condensed phase, e.g., the study of ultrafast chiral-specific dynamics in molecules, ultrafast chiral recognition via photoelectron circular dichroism [19,43], ultrafast magnetization and spin

dynamics [44–46], etc.

While the potential of high harmonic generation in bi-circular fields as a light source is actively explored, the complementary *spectroscopic* potential of this scheme for studying the underlying electronic dynamics and dynamical symmetries is far less known. Pertinent recent papers include Refs. [19, 34, 36, 38]. This situation stands in stark contrast to the two-dimensional high harmonic spectroscopy which uses the combination of linearly polarized fundamental and its second harmonic [11, 13–18, 47–53], allowing one to track electronic and vibronic [13] dynamics with temporal resolution from tens of femtoseconds down to tens of attoseconds.

Here we demonstrate the spectroscopic potential of high harmonic generation in bi-circular laser fields to track light-driven dynamical symmetry breaking in a quantum system. In general, the emergence of strong, symmetry forbidden, lines in high harmonic spectra is a tell-tale sign of symmetry breaking induced by the underlying attosecond electronic [54, 55] or vibronic dynamics [56–58]. Specifically, we show that symmetry forbidden lines in high harmonic spectra generated in bi-circular fields are sensitive to frustrated tunnel ionization [59–64] and the presence of strongly laser-driven Rydberg states, the so-called ‘bound states of the free electron’ [65], which are able to survive intense laser fields [60–64, 66–69] even when the ground state of the neutral is completely depleted [61, 70].

In contrast to single-color high harmonic spectroscopy of the dynamical symmetry breaking [54, 56–58], the two-color laser field offers clear advantages: it allows one to tune the time-delay between the two colors and their relative intensities. We rely on this ability in the present work. It allows us to make first steps towards addressing an extremely exciting but equally challenging problem of time-resolving the frustrated tunneling process [60, 61, 63, 71, 72] during the driving laser pulse.

The ability to control the shape of the driving field by changing the relative intensities of the two colors and their delay also brings up the complementary aspect of attosecond electron dynamics in multi-color fields – the ability to control these dynamics and the properties of the emitted radiation [14, 47–49, 52]. We explore this ability in the present work.

When a circularly polarized driver with frequency ω is used in combination with its counter-rotating second harmonic, the resulting field has the three-fold symmetry shown in Fig.1. As a consequence, high harmonic spectra generated in centrally symmetric media present peaks at the $3N + 1$ and $3N + 2$ harmonic lines, but not at $3N$. The $3N + 1$ and $3N + 2$ harmonics are circularly polarized and rotate in the directions of the ω and 2ω fields, respectively. The $3N$ harmonic lines are symmetry forbidden, their lack reflecting the conservation of the angular momentum. Indeed, these lines correspond to the absorption of the net amount N of the fundamental $\hbar\omega$ photons and the net amount N of the second harmonic $2\hbar\omega$ photons, i.e. the net total of $2N$ photons, preserving the parity of the initial state and thus precluding one-photon radiative recombination to it.

In spite of this clear symmetry argument, non-negligible signals at $3N$ harmonic lines have been routinely observed in experiments, starting with the pioneering work [28]. Their presence has been systematically ascribed to slight ellipticity of the drivers. While this is certainly an important experimental reason, it is not the only one, as has been recently highlighted by Baykusheva [34]. The emergence of strong forbidden lines can manifest the lack of symmetry of the quantum system, in particular the destruction of the dynamical symmetry within the laser cycle (Fig.1). This makes the analysis of the forbidden lines, ideally in a time-resolved fashion, very interesting, opening a route to time-resolving the changing symmetries of the quantum system.

Turning from the spectroscopic aspect of high harmonic generation to the light-source aspect, it is also important to understand the origin of the forbidden lines, the mechanisms controlling their strengths and polarization. Indeed, these lines will play crucial role in determining the polarization properties of attosecond pulses or pulse trains produced by the combination of circularly polarized high harmonics generated in a bi-circular field.

Addressing these issues is the focus of this paper. In particular, we find theoretically that small deviations from perfectly circular light $\epsilon = 1.0$, e.g. $\epsilon = 0.95$, which would be typical for realistic experiments, is hardly the main reason for their prominence. Thus, the emergence of strong forbidden lines in standard experiments with nearly circular pulses is rather unexpected and cannot be blamed entirely on small deviations from perfect circularity.

To uncover the physics responsible for the $3N$ lines, we study the case when the two pulses constituting the bicircular field, ω and 2ω , are time-delayed but still overlap. This allows us to track the emergence of the $3N$ lines as a function of the $\omega - 2\omega$ delay. Using Helium as a target gas and the combination of 800 nm and 400 nm driving fields, we find experimentally and theoretically that the $3N$ lines become stronger as the delay between the two pulses increases and their overlap decreases, especially when the 2ω (400 nm) pulse comes first.

It is well known that, in contrast to 800 nm, the 400 nm pump leads to efficient accumulation of population in Rydberg states via frustrated tunnelling (see e.g. [64] for detailed experimental and theoretical analysis), and that these states survive strong dressing fields [60, 61, 63, 71, 72]. Thus, our results suggest that in the pump-probe type setup, when the 800 nm pulse is delayed, the 400 nm field excites the bound states and breaks the dynamical symmetry due to sub-cycle accumulation of population in these states. Since frustrated tunnelling in the 800 nm field is less efficient than for 400 nm field [64], the dynamical symmetry breaking should be weaker when the 800 nm pulse comes first. This expectation is confirmed by our observations: the forbidden $3N$ lines are more prominent when the 400 nm pulse precedes the 800 nm pulse.

The importance of Rydberg excitation is further tested experimentally by changing the intensity of the 400 nm pulse. In agreement with the above physical picture, we find that the forbidden lines become more prominent with higher intensity of the 400 nm light. Theoretically, even for perfectly circular pulses, the forbidden harmonic lines appear in a dramatic way if the intensity of the 400 nm field is increased substantially above the fundamental. In contrast, raising the 800 nm intensity does not have the same effect.

We further confirm this physical picture by showing how the gradual build up of the forbidden lines in the spectrum. Thus, from the high harmonic spectroscopy perspective, analyzing the appearance of the forbidden harmonics as a function of the ω - 2ω delay and intensities, we make first steps towards seeing how the frustrated tunneling process [60, 61, 63, 71, 72] unfolds in time.

From the light source perspective, we analyze the unusual polarization properties of the $3N$ lines and show the ways of controlling their strength and ellipticity: by varying the two-color delay or the relative intensities of the two driving fields. The intensities and the polarization properties of these lines are important in determining the polarization properties of the attosecond pulse trains produced via high harmonic generation in bi-circular fields.

Dynamical symmetry and the selection rules

Consider high harmonics generated by the two counter-rotating circular pulses with frequencies ω and 2ω . We write the total electric field as

$$\mathbf{E}(t) = \sqrt{2} \operatorname{Re} \left\{ -F_{\omega} e^{-i\omega t} \hat{\mathbf{e}}_{+} + F_{2\omega} e^{-i2\omega t} \hat{\mathbf{e}}_{-} + 0 \hat{\mathbf{e}}_0 \right\}. \quad (1)$$

The three components of the field correspond to the counter-clockwise ($\hat{\mathbf{e}}_{+} = -(\hat{\mathbf{e}}_x + i\hat{\mathbf{e}}_y)/\sqrt{2}$) and clockwise ($\hat{\mathbf{e}}_{-} = (\hat{\mathbf{e}}_x - i\hat{\mathbf{e}}_y)/\sqrt{2}$) rotations in the x - y plane, and a linear component ($\hat{\mathbf{e}}_0 = \hat{\mathbf{e}}_z$) along the z axis. For collinear driving fields, which we assume in this work, the latter is always zero. The fundamental field rotates in the counter-clockwise, positive direction (polarization $\hat{\mathbf{e}}_{+}$), while the second harmonic rotates clockwise (polarization $\hat{\mathbf{e}}_{-}$).

The inset in Fig 1d shows the total field, which has characteristic three-leaf structure. The total field rotates counter-clockwise, from the leaf $k = 1$ aligned horizontally, along the x -axis, to the leaf $k = 2$ turned 120 degrees counter-clockwise, to the leaf $k = 3$ turned 240 degrees counter-clockwise. Each leaf generates a burst of emission. To simplify the discussion and notations,

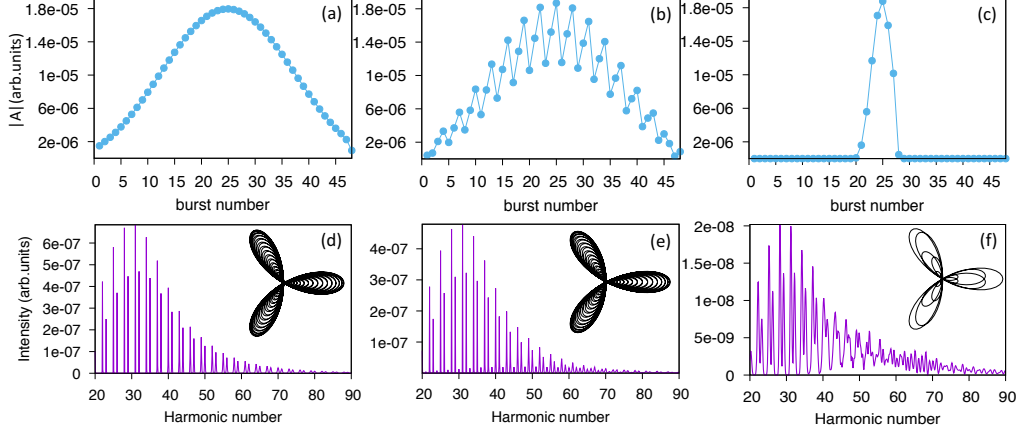


Fig. 1. **Typical harmonic spectra in bi-circular fields.** Strong field approximation solutions for the bicircular scheme using a short-range potential with an ionization potential of $I_p = 24.6$ eV (as helium). In the top row, the amplitude distribution of the different bursts, temporally ordered, that contribute to an arbitrary high harmonic (H60). In the bottom row, the HHG spectra. The fields are Gaussian-shaped, with a peak intensity of $I = 3.5 \times 10^{14}$ W/cm², and duration of: (a,d) 38 fs, (b,e) 38 fs with an ellipticity of 0.9, and (c,f) 6 fs. The Lissajous figures of the corresponding fields are shown in the top right corners of the bottom panels.

but without the loss of generality, we consider emission associated with the so-called short trajectories [73]. In bicircular fields, their contribution on the single-atom level is dominant [29]. Within each cycle of the fundamental field, the emission contains three bursts, each associated with one of the three leaves of the total field and labelled by the index $k = 1, 2, 3$. The corresponding induced dipoles are

$$\mathbf{d}^{(k)}(t) = \mathbf{A}_+^{(k)}(t) e^{i\phi_+^{(k)}(t)} \hat{\mathbf{e}}_+ + \mathbf{A}_-^{(k)}(t) e^{i\phi_-^{(k)}(t)} \hat{\mathbf{e}}_- . \quad (2)$$

Each dipole has components with both polarizations, $\hat{\mathbf{e}}_{\pm}$, and each component is carrying its own amplitude and phase. As always in strong-field driven high harmonic generation, the phase is dominated by the action accumulated during the motion of the electron in the continuum, while the amplitude is dominated by strong-field ionization conditioned on the electron return to the vicinity of the parent ion. Note that the two-color driving field curves the electron trajectory. This curved continuum motion imposed by the field means that the recombination dipole matrix elements will be different for the emission of photons co-rotating and counter-rotating with the fundamental laser field.

If the circular pulses at the frequencies ω and 2ω are long and overlap perfectly, then a rotation of $2\pi k/3$ (with k integer) leaves the field invariant (see Fig. 1). This three-fold symmetry of the field, together with the symmetry of the medium, imply that the phases and the amplitudes for $k = 2, 3$ are the same as for $k = 1$, up to the $2\pi/3$ and $4\pi/3$ rotations of the associated vectors $\hat{\mathbf{e}}_{\pm}$ for $k = 2$ and $k = 3$, and the time-delay of the emission bursts by $1/3$ and $2/3$ of the laser cycle correspondingly. Under rotation by an angle α , the $\hat{\mathbf{e}}_{\pm}$ vectors transform as

$$\begin{aligned} \hat{\mathbf{e}}_+ &\rightarrow \hat{\mathbf{e}}_+ e^{-i\alpha} \\ \hat{\mathbf{e}}_- &\rightarrow \hat{\mathbf{e}}_- e^{+i\alpha} . \end{aligned} \quad (3)$$

Upon the Fourier transform into the frequency domain, the contributions from each leaf will gain additional phases $\exp(iMk2\pi/3)$ from the $\exp(iM\omega t)$ factor in the Fourier integral, due to the corresponding time-delays in emission by $\omega t = k2\pi/3$. Hence, the total contribution of the three

bursts to the emission dipole at the frequency $M\omega$ is, for the component co-rotating with the fundamental field,

$$\mathbf{d}_+(M\omega) = \mathbf{A}_+(M)e^{i\phi_+(M)}\hat{\mathbf{e}}_+ \left[1 + e^{-i2\pi/3+iM2\pi/3} + e^{-i4\pi/3+iM4\pi/3} \right] \quad (4)$$

Similarly, for the component of the harmonics which co-rotates with the second harmonic, we have

$$\mathbf{d}_-(M\omega) = \mathbf{A}_-(M)e^{i\phi_-(M)}\hat{\mathbf{e}}_- \left[1 + e^{+i2\pi/3+iM2\pi/3} + e^{+i4\pi/3+iM4\pi/3} \right] \quad (5)$$

For the intensities $I_{\hat{\mathbf{e}}_{\pm}} \propto |\mathbf{d}_{\pm}(M\omega)|^2$ we obtain

$$\begin{aligned} I_{\hat{\mathbf{e}}_+}(M\omega) &\propto 3 + 2 \cos [2\pi(M-1)/3] + \cos [4\pi(M-1)/3], \\ I_{\hat{\mathbf{e}}_-}(M\omega) &\propto 3 + 2 \cos [2\pi(M+1)/3] + \cos [4\pi(M+1)/3]. \end{aligned} \quad (6)$$

The expressions Eqs.(4,5,6) show the symmetry-imposed selection rules for the harmonics of different polarization. We stress again that these rules assume that three emission bursts associated with the three leaves of the driving field are identical, up to rotation and time-delay.

The counter-clockwise component, co-rotating with the red field, will be enhanced for the $M = 3N + 1$ harmonics and cancelled by the interference of the three terms for the $M = 3N + 2$ harmonics. The clockwise component, co-rotating with the blue field, will be enhanced for the $M = 3N + 2$ harmonics and cancelled by the interference of the three terms for $M = 3N + 1$ harmonic. Finally, the $M = 3N$ harmonics will be always suppressed (provided the fields are propagating collinearly), giving rise to the characteristic HHG spectrum of the $\omega + 2\omega$ scheme [28, 29](Fig. 1d). Fig. 1(a) shows the calculated amplitudes $|A|$ of the different emission bursts for a given harmonic (we have used $M = 60$ in this Figure) using an ellipticity of 1.0 in both fields, in the case when the two driving fields have identical pulse durations and overlap perfectly. The calculations are based on using the saddle point method and the standard strong field approximation (SFA), following Milošević and Becker [29] and considering the contribution of the saddle points associated with the short trajectories in the bicircular field. The ionization potential was set to $I_p = 24.6$ eV (Helium), with the ground s-state being the initial state. The driving pulses are both Gaussian-shaped, with a peak field strength of $F_\omega = F_{2\omega} = 0.1$ a.u., and duration of (a,d) 38 fs. The harmonic spectrum, shown in Fig. 1(d), demonstrates the lack of $M=60$ and all harmonics with orders $M = 3N$. Interestingly, the lines $M = 3N + 1$ and $3N + 2$, with opposite helicity, have different heights, even though we used the ground s-state. This propensity reflects the curvature of the motion imposed on the electron between ionization and recombination. Here, the curvature is dominated by the fundamental field.

Physical origin of the forbidden harmonics

Several factors can alter the simple selection rules associated with the three-fold dynamical symmetry of the driving field. Two possibilities lie on the surface and are illustrated in Fig. 1(b,c,e,f).

First, if the pulses are elliptical rather than perfectly circular, the field will not be invariant under a $2\pi/3$ rotation anymore. Fig. 1b shows the amplitudes $|A|$ for a given harmonic (we have used $M = 60$ in this Figure) the different emission bursts, but now for the ellipticity of 0.9 (for both fields). To eliminate other possible mechanisms responsible for the $3N$ lines and focus on the role of ellipticity, the calculations used the strong field approximation (SFA) approach for the bi-circular fields [29]. One of the bursts inside the cycle is stronger than the other two, leading to the appearance of the forbidden harmonics in the spectrum (see Fig. 1(e)) This asymmetry in the driving field is hardly visible in Fig. 1(e) inset, but becomes noticeable in the harmonic amplitudes due to exponential sensitivity of tunnel ionization to the field. Nevertheless, the

forbidden lines are quite weak, even for these rather substantial deviations from the perfectly circular driving fields.

Second, for short pulses, many of the bursts will be strongly suppressed by a rapidly changing envelope. Their amplitudes and phases, for a specific harmonic, will depend on the rapidly changing fields at the times of ionization and recombination. In particular, this leads to a heavily non-symmetric amplitude distribution with respect to the central (more intense) burst, as can be seen in Fig. 1(c), again for H60. This loss of symmetry can be observed in the HHG as a signal at the forbidden harmonic lines. These indeed arise prominently for H60 and higher orders (Fig. 1(f)).

There are, however, two additional, more subtle, possibilities of breaking the dynamical symmetry that are crucial in this work. First, a memory present in the quantum system would make the contributions from successive peaks of the field different. This is in analogy to XUV-assisted high harmonic generation in linear fields [74], where an XUV pulse pumps the system to a superposition of Rydberg states, from which ionization occurs easier. In this case, the 400 nm pulse acts as a multi-photon pump which excites the system into a superposition of Rydberg states. Ionization in the subsequent bursts is therefore enhanced and hence $A_{+/-}^{(1)} \neq A_{+/-}^{(2)} \neq A_{+/-}^{(3)}$, which breaks the dynamical symmetry. Second, one can vary the time delay between the two driving pulses, the fundamental and the second harmonic, breaking the symmetry of the total field in a well controlled way. For the two circular driving fields, high harmonic signal will only be produced in the region of their overlap. Time delaying one of the two pulses leads to the asymmetric behaviour of the successive emission bursts, similar to a short two-color pulse. We use the interplay of these two possibilities in our analysis below.

The physical idea is as follows: the system memory is linked to the excitations generated by the driving pulse. The efficiency of the excitations by the second harmonic field is higher than by the fundamental. Hence, memory effects and the strengths of the forbidden harmonics should be more prominent when the second harmonic arrives first, compared to the case when the second harmonic arrives second. Thus, systematically varying the two-color delay and recording the relative strength of the forbidden lines allows us to gauge the role of the dynamical symmetry breaking associated with the memory of the quantum system.

Experimental setup

We have performed experiments in helium using a Ti:sapphire-based laser system with a single stage regenerative amplifier producing 38 fs pulses with up to 4 mJ energy and a central wavelength of ~ 795 nm at 1 kHz repetition rate. The carrier-envelope phase (CEP) of the pulses was not locked. The laser beam was directed into the optical setup shown in Fig. 2.

The original beam was split into two beams, with the possibility to use the splitting ratios of 50/50, 70/30 and 80/20. The first beam was directed into a BBO crystal to generate the second harmonic (at ~ 400 nm) with the pulse energy up to 0.8 mJ. The second beam, remaining at fundamental wavelength 795 nm, had the pulse energy up to 1.0 mJ. We could also smoothly tune the energies of the pulses and ratio between the ‘‘red’’ and the ‘‘blue’’ beams by changing the pump pulse energy in the amplifier.

Both beams passed through the corresponding achromatic broadband $\lambda/2$ and $\lambda/4$ waveplates, where their polarization was converted into nearly circular, with the ellipticity as high as $\varepsilon \simeq 0.95$. The optical path of the fundamental beam was controlled using a rooftop mirror mounted on a translation stage. The fundamental and the second harmonic beams were combined together in the collinear geometry and focused with a single Ag-mirror at $f/100$ into a 5-mm-long gas cell containing helium.

The waists of the fundamental and the second harmonic (red and blue) beams were measured to be $w_0(\omega) \simeq 33 \mu\text{m}$ and $w_0(2\omega) \simeq 27 \mu\text{m}$ respectively, so that the maximum intensity could reach as high as $I_\omega \sim 9.0 \times 10^{14} \text{ W/cm}^2$ and $I_{2\omega} \sim 7.2 \times 10^{14} \text{ W/cm}^2$. The pulses were

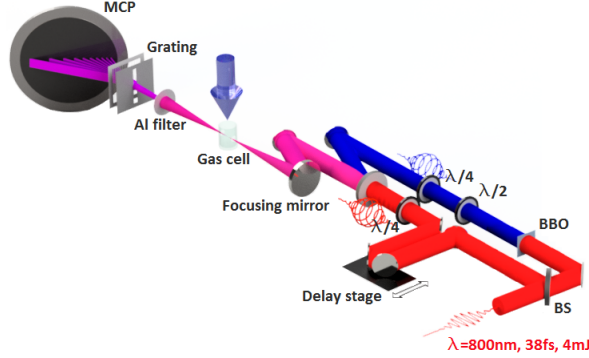


Fig. 2. **Experimental layout.** BBO: beta-barium-borate crystal for second harmonic generation, MCP: multi-channel plate based detector for XUV radiation, BS: beam-splitting, partially transmitting mirror.

focused approximately 2 mm before the target, minimizing the contribution of the Gouy phase to macroscopic effects and selecting short electron trajectories. The gas cell, placed inside the vacuum chamber, was initially sealed with a metal foil. The foil was burned through by the laser beam at the start of the experiment. The resulting cell opening had the size $d = 40 \mu\text{m}$ similar to the spot size on the cell position, allowing us to keep the gas pressure inside the cell constant at $\approx 40 \text{ mbar}$ at the appropriate level of vacuum (typically $P_{\text{rest}} \approx 10^{-4} \text{ mbar}$) inside the interaction chamber.

After passing the 5 mm gas cell, the driving ‘red’ and ‘blue’ beams were blocked by an 300 nm thick aluminum foil. The transmitted XUV radiation was directed towards the XUV spectrometer placed insight the vacuum chamber differentially separated from the interaction chamber. The XUV-spectrometer was based on the silicon nitride transmission nanograting operating in the wavelength range of 10 to 80 nm [75] with a resolution of 0,25 – 0,13 nm across the whole spectral range. The generated and spectrally resolved XUV radiation was detected by a double-microchannel plate (MCP) with a phosphor screen and recorded by a fast CMOS camera (PointGrey). Radiation up to harmonic orders ~ 50 was observed.

Experimental results

Fig. 3 shows the observed XUV-spectra, for the bi-circular driving field and different red-blue time-delays. When the two driving pulses overlap (see Fig. 3 (b)), the harmonics with order $3N$ are suppressed.

We have measured and analysed the XUV spectra as a function of the time delay between the 800 nm and the 400 nm pulses. The time zero of the perfect overlap between the two pulses was determined via the cross-correlation between the two beams in the BBO crystal, with the measured cross-correlation length $\approx 40 \text{ fs}$. The positive time delay means that the second harmonics arrives after the fundamental.

While the experimentally observed spectra are likely affected by the macroscopic propagation effects, we focus on the features that must originate in the single-atom response: the dependence of the forbidden harmonic lines on the delay and the relative intensities of the two driving fields. Obviously, macroscopic propagation cannot lead to the appearance of forbidden harmonics if they are not generated at the single-atom level.

From this perspective, the main features in the experimental spectra in Fig. 3 are as follows. First, we see the appearance of the forbidden $3N$ harmonics when we increase the time-delay between the two pulses, while at $\tau=0$ these harmonics are very strongly suppressed. Second, the

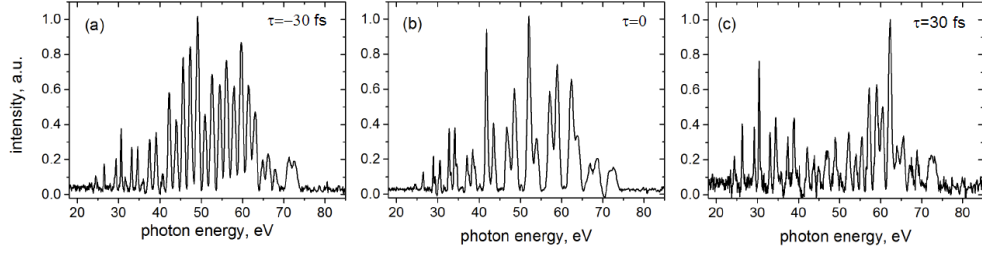


Fig. 3. **Experimental spectra.** Experimental XUV-spectra generated in the bi-circular field as a function of the $\omega - 2\omega$ pulses time delay τ (negative delay corresponds to the blue pulse arriving first): (a) $\tau = -30$ fs (close to 40 fsec cross-correlation length), (b) $\tau = 0$ fs, (c) $\tau = 30$ fs.

$3N$ harmonics are a lot more prominent for the negative time delay, i.e. when the blue pulse arrives first. This experimentally observed feature was found to be robust with respect to varying the intensities of the two-color laser field.

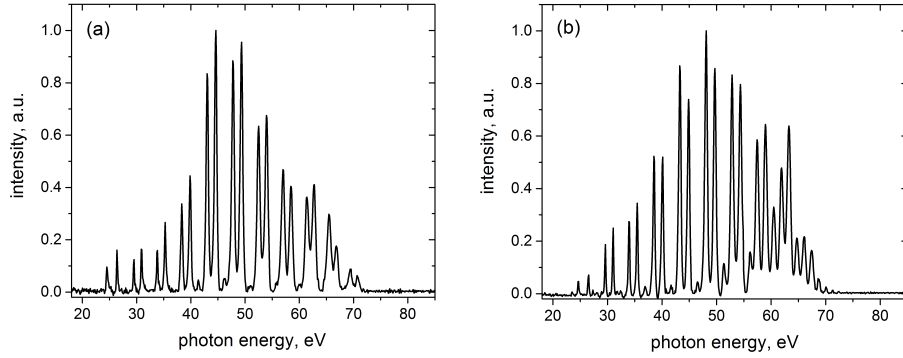


Fig. 4. **Experimental spectra.** Experimental XUV-spectra generated in the bi-circular field at $\tau = 0$ fs. Panel (a): stronger red field, $I_\omega \sim 5 \times 10^{14}$ W/cm², $I_{2\omega} \sim 4 \times 10^{14}$ W/cm²; Panel (b): stronger blue field, $I_\omega \sim 5 \times 10^{14}$ W/cm², $I_{2\omega} \sim 6 \times 10^{14}$ W/cm²

Fig. 4 shows how changing the light intensity, especially the ratio between the fundamental and the second harmonic, affects the high harmonic spectrum. Apart from the clear effect of absorption in the lower energy region and the expected trend that higher intensities leads to higher harmonic cut-offs, we again bring the reader's attention to the forbidden $3N$ orders. We observe, that the forbidden $3N$ harmonics are effectively suppressed when the fundamental field is stronger than the second harmonic (Fig. 4a), or when the two intensities are close to each other (Fig. 3b). When the intensity of the 400 nm pulse is higher than that of the 800 nm pulse, however, the forbidden harmonics become prominent (Fig. 4b). These observations again seem to confirm the idea that frustrated tunneling is playing a prominent role.

Numerical Results

We now turn to numerical simulations to reinforce this physical idea and rule out propagation effects. The strong field approximation, which neglects the excited states, is not adequate for the analysis, and we solve the time-dependent Schrödinger equation for the Helium atom.

We used the code described in [76]. To simulate the helium atom, we used the 3D single-active electron pseudo-potential given in [77]. We have used a radial box of 600 a.u., with a total number of points $nr = 1535$. We use a uniform grid, with 33 points (grid spacing of 0.14 a.u.) at the origin, followed by 34 points on a logarithmic grid, with a scaling parameter of 1.03, starting at 5 a.u., and finally 1468 points on a uniform grid with a spacing of 0.4 a.u. We placed a complex boundary absorber at the border of the radial box (starting at 470 a.u.), in order to avoid reflections. However, the box is sufficiently large to contain the full wave-function at the end of the pulse (we check that the total norm in the simulation volume is 1.0 at the end of the pulse). Therefore we can apply the iSURFC method [78]. The maximum angular momenta included in the spherical harmonics expansion was $\ell_{\max} = 70$. The time grid had a spacing of $dt = 0.04$ a.u. All the discretization parameters have been checked for convergence.

Fig. 5 shows our results obtained for 20 fs Gaussian pulses with intensities $I_{\omega}^{\text{th}} = I_{2\omega}^{\text{th}} = 0.12$ PW/cm², corresponding to the peak fields of $F_{\omega}^{\text{th}} = F_{2\omega}^{\text{th}} = 0.058$ a.u., with variable time delay of $\tau = -16, 0, 16$ fsec. The center of the fundamental pulse is fixed at $t_{0,\omega} = 0$, and $\tau = t_{0,2\omega}$ marks the center of the second harmonic pulse. Positive τ means that the second harmonic pulse comes later, negative τ means that it comes earlier. The top row shows the x-component of the total field, while the other rows show the harmonic spectra and the ratio between the forbidden and permitted lines. The spectra are presented for both perfectly circular (panels d-f) and elliptic $\epsilon = 0.9$ (panels j-l) fields, and the intensities of the two fields are equal.

As expected, the $3N$ lines are suppressed for $\tau = 0$ but become stronger as we increase time delays between the two pulses. Crucially, the ratio $R(\tau) = S_{3N}(\tau)/S_{3N+1}(\tau)$ (panels g-i in Fig. 5) is asymmetric as a function of τ , strongly suggesting that the memory of the quantum system is playing a role, i.e. the blue pulse excites the system and the delayed red pulse probes the excitation. The effect is common for both perfectly circular and elliptic fields, with the pulse ellipticity playing a secondary role in the effect.

We now focus on perfectly circular and perfectly overlapping pulses and show how the forbidden harmonics arise even in these cases, thanks to the role of strongly driven Rydberg states trapping population during strong field ionization. To this end, we have performed theoretical simulations with perfectly circular, overlapping pulses of 12 fs FWHM duration for three different ratios of the field strengths, see Fig. 6. The ratio $F_{2\omega}/F_{\omega}$ is varied from $F_{2\omega}/F_{\omega} = 2/3$ (c) through $F_{2\omega}/F_{\omega} = 1$ (b) to $F_{2\omega}/F_{\omega} = 3/2$ (a). The total intensity and, hence, the peak of the total electric field are kept constant for (a) and (c), $I_{\max} = I_{2\omega} + I_{\omega} = 3.7 \times 10^{14}$ W/cm², and is lowered for (b), $I_{\max} = I_{2\omega} + I_{\omega} = 2.4 \times 10^{14}$ W/cm².

Substantial $3N$ lines such as $H24, H27, H30$ and especially $H33$ appear when the second harmonic is stronger than the fundamental ($F_{2\omega} = (3/2)F_{\omega} = 0.085$ a.u.) and dominates ionization, see panel (a). When the strength of the fundamental field field strengths are equal ($F_{2\omega} = F_{\omega} = 0.057$ a.u.), panel (b), or when the fundamental is stronger ($F_{2\omega} = (2/3)F_{\omega} = 0.038$ a.u.) the $3N$ harmonics are essentially absent.

To understand the reason behind this breaking of the symmetry, we projected the wavefunction at the end of the pulse onto the bound states of the atom. In Fig. 6d we show the bound population of the first seven excited states (excluding the ground state), sorted by total angular momentum, at the end of the pulse. When the blue field is stronger than the red field, irrespective of the maximum peak intensity, the bound state population is dramatically higher. In the energy domain (multiphoton) picture, this is the consequence of fewer high energy photons needed to resonantly populate the higher lying states. In the time-domain (tunneling) picture, when the blue field dominates ionization, the electron orbit is more likely to be trapped – the frustrated tunnelling is more efficient at 400 nm than at 800 nm.

This picture is confirmed in Fig. 7, where we show six snapshots of how the spectrum in Fig. 6a and 6c builds with time. To do this, we apply a gradually increasing window function to the time-dependent induced dipole $D(t) = \langle \Psi(t) | \hat{d} | \Psi(t) \rangle$. The upper panel shows the length of

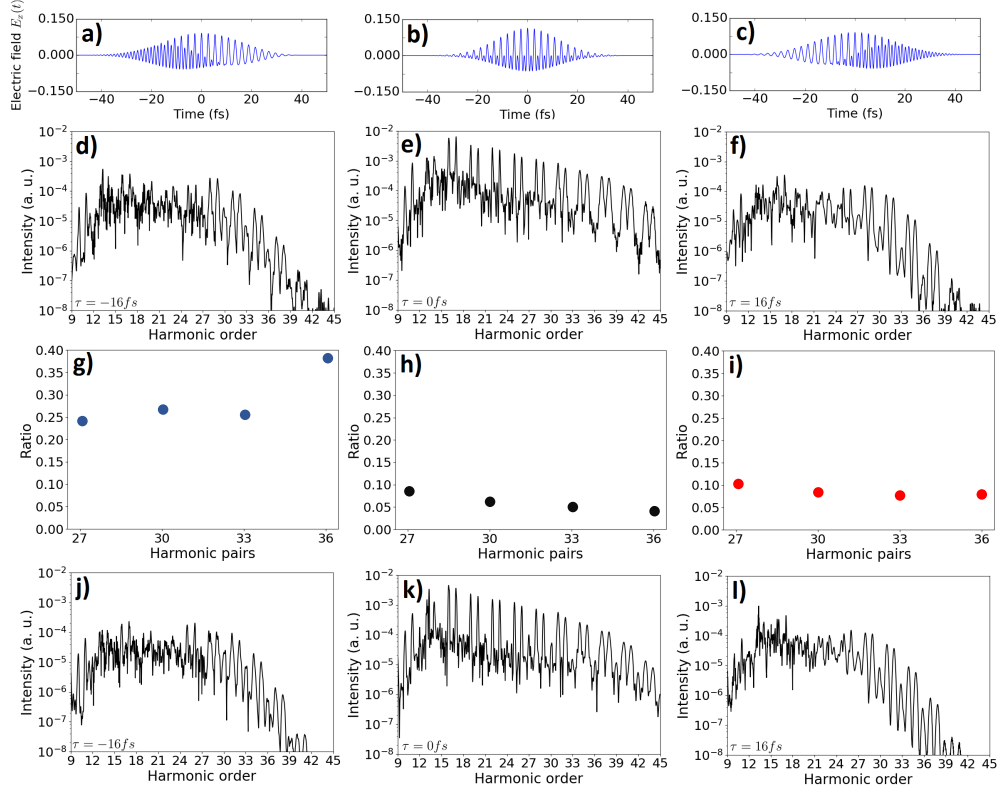


Fig. 5. **Theoretical HHG spectra as a function of the blue-red time delay.** Top row: x-component of the bicircular field; second row: spectra for perfectly circular driving pulses; third row: ratio of the forbidden $3N$ harmonic to its $3N+1$ neighbor; fourth row: spectra for elliptical pulses, $\epsilon = 0.9$. Left column: the 400 nm pulse comes first; middle column: perfect overlap; right column: the 400 nm pulse is delayed.

this temporal window as the shaded area, along with the total intensity $F_x^2 + F_y^2$ of the $\omega + 2\omega$ laser field (red line). The central and bottom panels show the corresponding spectrum for that energy window for the cases when the 400 nm field is stronger or weaker than the 800 nm field, respectively.

Early on, Fig. 7(a), the lower harmonics show only symmetry-allowed harmonics. For the higher harmonics, there is not yet enough time to provide a sequence of consecutive bursts with sufficient energy, which would interfere to yield clear harmonic lines. The forbidden harmonics are absent or very low in both spectra, indicating that the excited states are not sufficiently populated to play any significant role. As we increase the temporal window (Fig. 7b), the excited states start to get populated when the blue field is stronger, and the electrons begin to get trapped in trajectories orbiting around the ionic core. The forbidden harmonics start to emerge when the blue field is stronger, but not when the red is stronger. The prohibited lines appear first at higher harmonics. As we keep increasing the temporal window (Fig. 7c), lower harmonics start to show the forbidden lines.

More importantly, with increased time resolution the forbidden lines such as H30, H33 or H36 in Fig. 6c start to show a doublet structure. This is a characteristic feature of symmetry-forbidden lines, known for single-color fields [54] and demonstrating the population of more than one Floquet state during the laser pulse. As time keeps increasing and the field becomes stronger,

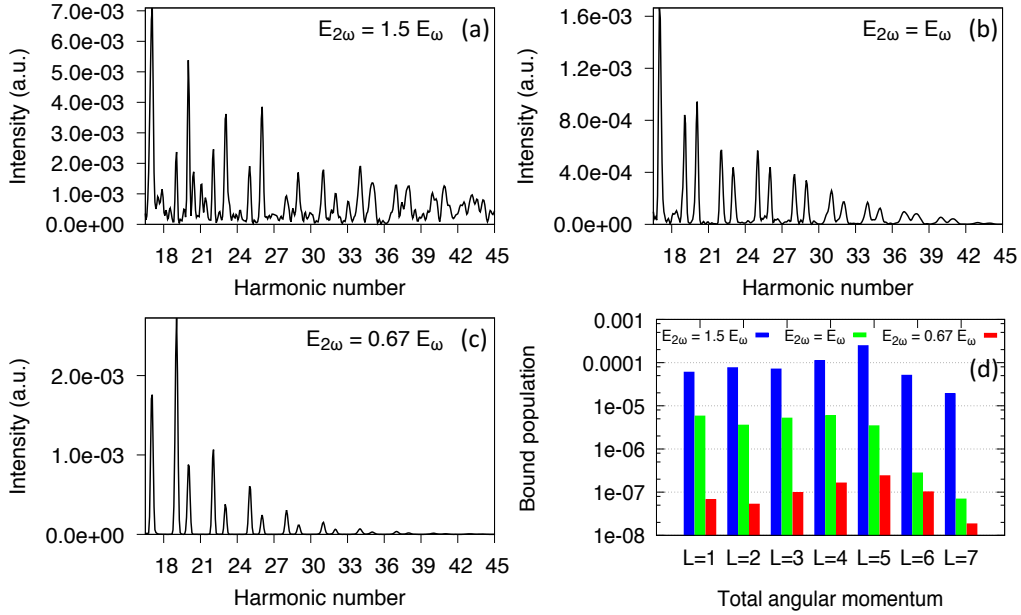


Fig. 6. **Influence of bound state population.** High harmonic spectrum of helium generated by two counter-rotating 12 fs long fields of frequencies 1.55 eV and 3.1 eV, for three different ratios of the field strengths: (a) $F_{2\omega} = 3/2F_{\omega} = 0.085$, (b) $F_{2\omega} = F_{\omega} = 0.057$, and (c) $F_{2\omega} = 2/3F_{\omega} = 0.038$. Peak intensities are the same for (a) and (c) and it is lower for (b), see text for details. Panel (d) shows the population of the bound states of the atom (in logarithmic scale) after the interaction with the field, for the three intensity ratios.

the doublet lines start to appear also for lower harmonics (see H18 and H21 in Fig. 7d and H6 and H9 in Fig. 7e). Higher harmonics now start to show a more complex structure, suggesting that multiple Floquet states are being populated by the rapidly changing field. While similar arguments are applicable for the case in which the red field is stronger, and indeed the forbidden harmonic lines are observable, the strengths of the signal is orders of magnitudes smaller due to the very small population of the excited states in the first place.

This information can be partially accessed experimentally by time-delaying the driving pulses. When the overlap between the two pulses is small, the spectrum should be similar to that in the case of the the short Fourier transform window, Fig. 7a. As the overlap of the pulses increases, the spectrum features will build up as in Fig. 7. With the blue pulse coming first, the excited population will be higher, leading to more prominent forbidden lines as discussed in the previous section.

In conclusion of the theoretical analysis, we also point out that varying the time delay between the two driving pulses allows us to control not only the strength of the forbidden harmonics, but also their ellipticity. Here we define the ellipticity as

$$\epsilon = \frac{I_{\hat{e}_+} - I_{\hat{e}_-}}{I_{\hat{e}_+} + I_{\hat{e}_-}}. \quad (7)$$

In Fig. 8 we show how this value changes as a function of the time delay for the four most visible forbidden harmonics in the spectrum: 30, 33, 36 and 39. A clear trend is observed. The forbidden harmonics rotate preferentially with the field that comes first, thus providing a mechanism to coherently control their ellipticity.

Finally, we also observe strong blue-shift for higher harmonics when the blue light comes first. As we can see from the field profile in the top panel of Fig. 5, in this case the more intense bursts

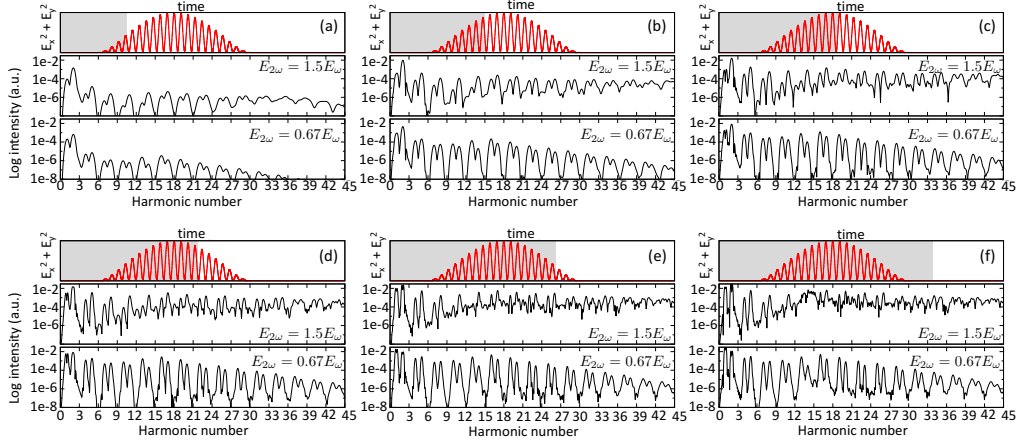


Fig. 7. **Build up of the spectrum.** Snapshots of the spectra in Fig. 6a (central panel) and Fig. 6c (bottom panel), at different times in the presence of the 12 fs long laser field: (a) 6 fs before the peak of the field, (b) 2.42 fs before the peak of the field, (c) 0.6 fs after the peak of the field, (d) 3 fs after the peak of the field, (e) 6.65 fs after the peak of the field, and (f) 12.7 fs after the peak of the field. The upper panel shows the maximum intensity of the field, $I_{max} = F_x^2 + F_y^2$, which is always the same for the upper and lower spectra, as the red line, and the shaded area indicates the temporal window applied to the dipole to obtain the corresponding spectrum.

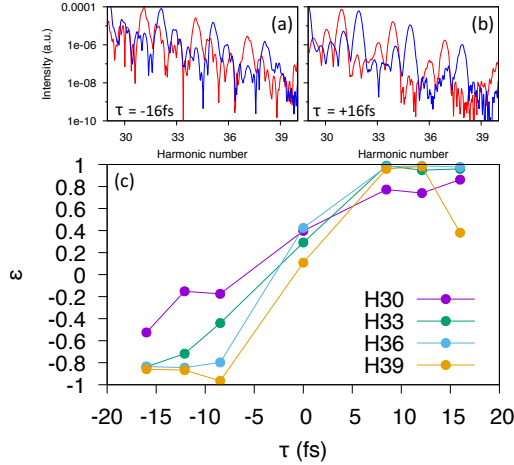


Fig. 8. **Ellipticity of the forbidden harmonics.** Top panels: Close-up of the theoretical HHG spectrum of the four most clearly observed forbidden high harmonics in the spectrum (30,33,36,39), for a time delay in which the blue field comes 16 fs before (a) and after (b) the red field. The red line indicates the intensity component that co-rotates with the red field, while the blue line indicates the component that co-rotates with the blue field. In panel (c), the value of the ellipticity (as defined by Eq. 7) of each of the four forbidden harmonics, as a function of the time delay. The points indicate the values for which there is data, and the lines are used to guide the eye.

are happen during the rising part of the field, leading to the blue shift of the harmonic lines just like in the case of linearly polarized few-cycle drivers. The opposite is true when red comes last. Indeed, a high harmonic H37 experiences a strong blue-shift of $E_{H37}(\tau = -16 \text{ fs}) - E_{H37}(\tau = 16 \text{ fs}) = 0.34 \text{ eV}$. The situation seems to reverse for lower harmonics. A lower harmonic H25 slightly red-shifts its position by $E_{H25}(\tau = -16 \text{ fs}) - E_{H25}(\tau = 16 \text{ fs}) = -0.12 \text{ eV}$. This provides a mechanism to fine tune the relative energy distance between harmonics.

Conclusion

In conclusion, we have shown the different mechanisms by which the forbidden harmonic lines may appear in the high harmonic spectrum generated by bicircular fields. In contrast to the commonly accepted wisdom that strong forbidden harmonics originate from slight ellipticity of the driving fields, we show that this is not the case. For ellipticities $\epsilon \approx 0.95$ dynamical symmetry breaking is too weak to be fully responsible for the strong forbidden lines. We have demonstrated that population of Rydberg states breaks the dynamical symmetry and leads to prominent signals at the forbidden harmonics.

The population of laser-driven Rydberg states is revealed by tracking the strength of the forbidden harmonic lines via the time delay between the two driving pulses. Increasing the intensity of the second harmonic field leads to stronger trapping of the electrons in high Rydberg orbits. In time domain, this is the consequence of the frustrated tunneling mechanism. In the frequency domain, they can be seen as the Freeman resonances [79, 80]. We have demonstrated that such dynamics are mapped on the forbidden harmonic lines that appear even for perfectly circular, long driving pulses.

We have temporally resolved these dynamics by applying a gradually increasing window function to the Fourier transform of the induced dipole, demonstrating the build-up of the forbidden harmonic lines as the excited states are populated on the rising edge of the laser pulse. Finally, in analogy with the blue-shift observed in the high harmonic generation triggered by short linearly polarized drivers, we have predicted and experimentally confirmed a substantial blue-shift of higher harmonics when the blue driver precedes the red driver.